UNIVERSAL WISER
PUBLISHER

Research Article

Radiative Impact on Jeffery Trihybrid Convective Nanoflow over an Extensible Riga Plate: Multiple Linear Regression Analysis

N Bhargavi ®, Poornima T*

Department of Mathematics, School of Advanced Sciences, Vellore Institute of Technology, Vellore, Tamilnadu-632014, India
Email: poornima.t@vit.ac.in

Abstract: Solar thermal systems utilize solar energy to generate heat, and the incorporation of nanoparticles such as Al_2O_3-Cu-Ni with a water base can elevate their efficiency. These nanofluids, composed of aluminum oxide, copper, and nickel nanoparticles dispersed in water, enhance heat absorption and transfer within the system. This improvement contributes to heightened overall performance and effectiveness of solar thermal systems. Cupronickel alloy helps in the process of desalination. Hence, this study examines the heat exchange properties in the context of a boundary layer flow of a trihybrid over a variable-thickness Riga plate stretched and heated by convective heat with non-Newtonian fluid (Jeffery) in the presence of thermal radiation. The governing equations of the boundary layer are transformed into a system of ordinary differential equations through appropriate similarity transformations, and those equations are resolved utilizing a boundary value problem program. The engineering parameters are analyzed through the application of multiple linear regression. The key finding of the investigation is that the Prandtl number, and thickness index number all have a positive impact on the Nusselt number. The presence of radiation and a uniform heat source improves the Nusselt number, physically this energy transfer improvement assists in higher solar collector efficacy; and converts that energy to usable heat. The rationale behind selecting trihybrid nanoparticles Al_2O_3, Cu, and Ni lies in the balance and inertness of Al_2O_3, with metals Cu, and Ni, both possessing more thermal conductivity.

Keywords: trihybrid nanofluid, solar thermal systems, multiple linear regression, thermal radiation, Jeffery fluid, riga plate

MSC: 35Q79

Nomenclature

Ha	Modified Hartmann number
Bi	Biot number
R	Thermal radiation parameter
λ	Heat source parameter
β	Dimensionless parameter to Riga plate
η	Dimensionless variable
ζ	Modified dimensionless variable

Θ	Dimensionless thermal function
Φ	Dimensionless concentration function
Pr	Prandtl's number
F	Dimensionless stream function
m	Thickness index
Je	Jeffrey parameter
Re_x	Local Reynold's number
Nu_x	Local Nusselt number

Dimensional parameters

μ	Dynamic viscosity (Pa.s)
α	Thermal diffusivity ($m^2.s^{-1}$)
ρ	Density ($kg.m^{-3}$)
v	Kinematic viscosity ($m^2.s^{-1}$)
α_1	Thickness parameter (s^{-1})
τ_w	Shear stress at the wall ($N.m^{-2}$)
k	Thermal conductivity ($W.m^{-1}.K^{-1}$)
Cp	Specific heat ($J.kg^{-1}.K$)
q_w	Heat flux ($W.m^{-2}$)
U_w	Stretching velocity ($m.s^{-1}$)
u, v	Horizontal and vertical velocity components ($m.s^{-1}$)
T	Temperature (K)
x, y	Cartesian coordinates (m)
a	Positive constant for stretching rate (s^{-1})

Subscripts

f	Base fluid
nf	Nanofluid
hf	Hybrid nanofluid
tf	Trihybrid nanofluid

1. Introduction

The thermal characteristics of convection-based heat transfer have significant importance in industrial and technical domains. Due to the poor thermal conductivity of several fluids, including kerosene, water, and oil, sufficient study must be done on the heat transfer mechanism. By incorporating nanoparticles into liquids and referring to them as "Nanofluids", it has been enhanced. Thermal conductivity and other rheological factors in typical nanofluids can now be improved by adding hybrid nanoparticles. The researchers created hybrid nanofluids to improve the heat transmission properties of the mono nanofluids. In many industrial applications, hybrid nanofluids have replaced mono nanofluids because mono nanofluids are incapable of providing the high thermal conductivity required for high heat flux devices. Hybrid nanofluids have dramatically altered the dynamics in industrial applications by lowering processing time, conserving energy, and extending the life of industrial equipment. All of this is feasible due to an increase in the rate of heat transmission of nanofluids. Several investigations [1-15] were conducted to demonstrate a considerable increase in the rate of heat exchange in instances of hybrid nanofluids under various situations. All these investigations inspired the researchers to develop more effective nanofluids with improved heat transfer and thermal conductivity. This resulted in the creation of a new working fluid, trihybrid nanofluid thought. A trihybrid nanofluid has three solid nanoparticles that are suspended in a base fluid. These are known as 'Modified nanofluids', 'Trihybrid nanofluids', and 'Ternary nanofluids', according to the researchers. In recent years, research has been undertaken to gain

a deeper understanding of the components that influence the heat transfer capabilities of such trihybrid nanofluid across diverse conditions. Revathi et al. [16] studied a quadratically stretching surface with second-order slip and Radiative heat exchange used to study the flow of a ternary hybrid nanofluid using multiple linear regression. Zayan et al. [17] studied the rheological properties of a water-based GO-TiO$_2$-Ag trihybrid nanofluid. Kumar et al. [18] investigated the numerical and experimental characteristics of an automobile radiator with a novel trihybrid nanofluid coolant. This investigation demonstrated a considerable improvement in the coolant's heat transfer coefficient and a greater engine fuel consumption rate. Algehyne et al. [19] studied the modified Buongiorno's model to examine how activation energy and bioactive mixers affect the chemically reacting jet flow of ternary hybrid nanofluid.

Because of their use in physiological and industrial processes, non-Newtonian rheological models have become more important than Newtonian fluids. It is noted that Newtonian fluids have only one constitutive relation; consequently, the real properties of complex fluids such as blood, oil, and polymer solutions cannot be determined using this model. To reveal the complex fluid characteristics, a wide range of rheological models, including the Jeffery, Johnson-Segalman, Eyring-Powell, Walters-B, second-grade, Sisko, FENE-P, PPT, Carreau-Yasuda, Casson, Eringen micropolar, Burgers' viscoelastic, Maxwell, and Sutterby fluid models, have been provided by multiple researchers. The importance of retardation and relaxing time is highlighted in the rate-type model. Jeffrey fluid, as introduced by Jeffrey, is a rate-type model. This model exhibits viscoelastic properties and has several uses in the polymer industry, as noted in [20-22]. Dharmaiah et al. [23] studied the nuclear reactor used on Jeffrey fluid flow with Falkner-Skan factor, non-linear thermal radiation, Brownian, and thermophoresis effects on the wedge. Garg et al. [24] studied the thermo-bioconvection movement of Jeffrey fluid including swimming microorganisms into an irregular porous medium.

The phenomena of heat transmission via the linear emission and absorption of electromagnetic radiation are referred to as thermal radiation. Electromagnetic waves are the sort of thermal radiation that is emitted by any object that is heated above absolute zero. This radiation is energy-carrying and can move heat across objects. Alnahdi et al. [25] examined the influences of radiation, dissipation, energy engagement, and tilted magnetized field related to hybrid nanofluid flow across a slick surface. Poornima et al. [26] determined the thermal radiation effects on non-Newtonian nanofluid flow through a flexible surface with a Newton boundary condition. Ramesh et al. [27] examined the impacts of radiation on Sutterby nanofluid via porous medium. Zhang et al. [28] studied the effect of quadratic and linear radiation on 3D convective hybrid nanofluid flow in a temperature-varying dissolution of fluids. Bhargavi et al. [29] investigated the impact of an electrically conducting and radiating liquid implanted in a porous media via a flat permeable plate on internal friction, heat generation, and thermal radiation.

According to our understanding of the literature, no research has been conducted on the movement of (Al$_2$O$_3$-Cu-Ni/H$_2$O) trihybrid nanofluid through an actively warmed Riga plate of varying thickness with non-Newtonian fluid in the presence of thermal radiation till now. As a result, the current study was developed to fill the research gap. The primary objective of this endeavor is to examine the parameters that improve the heat exchange of a (H$_2$O) base fluid mixed with (Al$_2$O$_3$, Cu, and Ni) trihybrid nanoparticles passing through an actively heated Riga plate of varied thickness with non-Newtonian fluid in the appearance of thermal radiation.

Multiple linear regression is employed to analyze and demonstrate technical characteristics such as friction factor and heat transfer rate. This work has applications in the condensation of extrusion of polymer sheets, aerodynamic extrusion of plastic sheets, metallic plates immersed in a cooling bath, Solar thermal systems, and many more. Tables and graphs are presented and briefly explained to demonstrate the influence of several relevant physical parameters on the heat exchange rate of the (Al$_2$O$_3$-Cu-Ni/H$_2$O) trihybrid nanofluid. Additionally, a noticeable rate of concordance is shown in the method of verification with the present findings and previous results. Solar thermal systems have various applications, including Solar water heaters utilizing the sun's energy to heat water for residential, commercial, or industrial use, reducing the need for conventional energy sources. Solar thermal systems can be integrated into buildings to provide space heating in colder climates or cooling through absorption chillers in warmer regions.

2. Formulation and geometry of the problem

In this study, Jeffery fluid flow of a (Al$_2$O$_3$-Cu-Ni/H$_2$O) trihybrid nanofluid past a stretching insuperable vertical Riga plate under changing width, thermal radiation, heat generation/absorption, and controlled convective heating as

shown in Figure 1. For Jeffery model, the relation for extra stress tensor is [30]:

$$S = \frac{\mu}{1 + \lambda_1} \left(A_1 + \lambda_2 \frac{dA_1}{d\bar{t}} \right)$$

With (λ_1, λ_2) Jeffery parameters, (μ) dynamic viscosity, and (A_1) first Rivlin-Ericksen tensor.
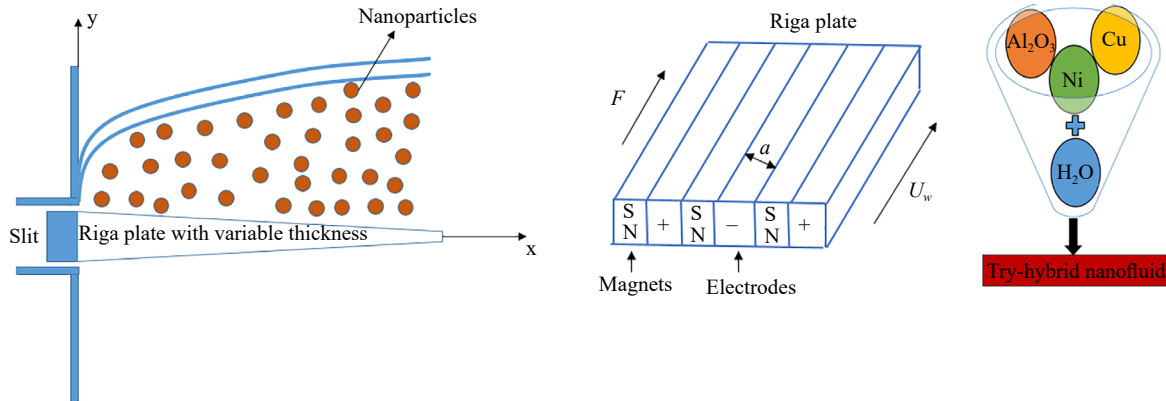

Figure 1. Physical model of the problem

Let us assume the following assumptions:

• The flow is steady and laminar.

• The Riga Plate's surface is considered to have varying thicknesses. This non-flatness is defined by the formula $y = A(x + b)^{(1 - m)/2}$, which differs depending on the distance from the origin. However, the thickness is thought to be unnoticeable to prevent unfavorable pressure gradient conditions.

• The Riga plate's stretching velocity has been calculated to be $U_w = U_0(x + b)^m$ where b is a number associated with the plate's stretching, m is the velocity exponent, and U_0 is a constant (when $b = 0$ and $m = 1$ represents a flat stretching sheet).

• Furthermore, assume that the induced magnetic field and the electric field formed because of charge separation are ignored in this study. Keeping the assumptions in mind, the appropriate governing continuity, momentum, and energy equations for the proposed model in Cartesian coordinates x and y are provided below [23, 31].

Continuity equation:

$$\frac{\partial u}{\partial x} + \frac{\partial v}{\partial y} = 0, \tag{1}$$

Momentum equation:

$$u \frac{\partial u}{\partial x} + v \frac{\partial u}{\partial y} = \frac{v_{tf}}{1 + Je} \frac{\partial^2 u}{\partial y^2} + \frac{\pi j_0 M}{8 \rho_{tf}} e^{-(\pi/a)y}, \tag{2}$$

Energy equation:

$$u \frac{\partial T}{\partial x} + v \frac{\partial T}{\partial y} = \alpha_{tf} \frac{\partial^2 T}{\partial y^2} + \frac{Q_0}{\left(\rho C_p \right)_{tf}} \left(T - T_\wp \right) - \frac{1}{\left(\rho C_p \right)_{tf}} \frac{\partial}{\partial y} \left(-\frac{4\sigma^* \partial T^4}{3k^* \partial y} \right), \tag{3}$$

The relevant boundary conditions are [31]:

$$u(x, y) = U_w = U_0(x + b)^m, \ v = 0, \ -k_{tf}\frac{\partial T}{\partial y} = h_s(T_w - T) \text{ at } y = A(x + b)^{(1-m)/2},$$

$$u \to 0, \ T \to T_\infty \text{ as } y \to \infty. \tag{4}$$

Similarity transformations are [31]

$$\psi = \left(\frac{2v_f U_0 (x+b)^{1+m}}{m+1}\right)^{1/2} F(\eta), \ \eta = y\left(\frac{(1+m)U_0(x+b)^{m-1}}{2v_f}\right)^{1/2}, \ \Theta(\eta) = \frac{T - T_\infty}{T_w - T_\infty}. \tag{5}$$

$$u = \frac{\partial \psi}{\partial y}, \ v = -\frac{\partial \psi}{\partial y}.$$

where ψ is a stream function and F, Θ are functions of η.

Using equation (5) satisfies continuity equation (1) and transformed equations (2-3) as

$$\frac{v_{tf}/v_f}{1+Je}F''' + FF'' - \frac{2m}{1+m}(F')^2 + \frac{2}{1+m}Hae^{-\beta\eta} = 0, \tag{6}$$

$$\frac{\alpha_{tf}}{\alpha_f}(R+1)\Theta'' + \Pr\left(\frac{2}{1+m}\Theta\lambda + F\Theta'\right) = 0, \tag{7}$$

The changed boundary conditions in (4) as

$$F(\alpha_1) = \alpha_1\frac{1-m}{1+m}, F'(\alpha_1) = 1, \ \frac{k_{tf}}{k_f}\left(\frac{1+m}{2}\right)^{1/2}\Theta'(\alpha_1) = -Bi\big(1 - \Theta(\alpha_1)\big),$$

$$F'(\infty) \to 0, \ \Theta(\infty) \to 0. \tag{8}$$

Here $\alpha_1 = A((1 + m)v_f/2a)$, and prime denotes the derivative with respect to η.

Let

$$F(\eta) = f(\eta - \alpha_1) = f(\zeta), \text{ and } \Theta(\eta) = \theta(\eta - \alpha_1) = \theta(\zeta). \tag{9}$$

With the use of equation (9) in equations (6-7) as

$$\frac{v_{tf}/v_f}{1+Je}f''' + ff'' - \frac{2m}{1+m}(f')^2 + \frac{2}{1+m}Hae^{-\beta(\zeta+\alpha_1)} = 0, \tag{10}$$

$$\frac{\alpha_{tf}}{\alpha_f}(R+1)\theta'' + \Pr\left(\frac{2}{1+m}\theta\lambda + f\theta'\right) = 0, \tag{11}$$

The changed boundary conditions in (8) as

$$f(0) = \alpha_1\frac{1-m}{1+m}, f'(0) = 1, \ \frac{k_{tf}}{k_f}\left(\frac{1+m}{2}\right)^{1/2}\theta'(0) = -Bi\big(1 - \theta(0)\big),$$

$$f'(\infty) = 0, \ \theta(\infty) = 0. \tag{12}$$

Where the prime notation signifies the derivative ζ.

The dimensionless parameters which obtained from above equations are

$$Ha = \frac{\pi j_0 M(x+b)}{U_w^2 8 \rho_{tf}}, \quad \beta = \frac{\pi}{a} \left(\frac{(1+m)U_0(x+b)^{m-1}}{2\nu_f} \right)^{-1/2}, \quad R = \frac{16\sigma^* T_\infty^3}{3k^* k_{tf}},$$

$$\lambda = \frac{Q_0(x+b)}{U_w(\rho C_p)_{tf}}, \quad \Pr = \frac{\nu_f}{\alpha_f}, \quad \text{and } Bi = \frac{h_s}{k_f} \left(\frac{U_0(x+b)^{m-1}}{\nu_f} \right)^{-1/2}. \tag{13}$$

The following are some significant engineering values:

$$Cf = \frac{\tau_w}{\rho_f U_w^2} \bigg|_{y=0}, \quad Nu = \frac{(x+b)q_w}{k_f(T_w - T_\infty)} \bigg|_{y=0}. \tag{14}$$

where

$$\tau_w = \frac{\mu_{tf}}{1+Je} \left(\frac{\partial u}{\partial y} \right), \quad \text{and } q_w = -k_{tf}(1+R) \left(\frac{\partial T}{\partial y} \right).$$

The dominant boundary conditions and similarity transformations are applied, and the resulting non-dimensional representations of the local Nusselt number and skin friction coefficient are as follows:

$$Cf(Re_x)^{1/2} = \frac{\mu_{tf} \left((1+m)/2 \right)^{1/2}}{\mu_f(1+Je)} f''(0), \quad Nu(Re_x)^{-1/2} = -\frac{k_{tf}(1+R) \left((1+m)/2 \right)^{1/2}}{k_f} \theta'(0). \tag{15}$$

Where $Re_x = \frac{U_w(x+b)}{\upsilon_f}$, is the local Reynold's number.

3. Numerical procedure

Dimensionless equations (10-12) are used to build a nonlinear boundary value problem. Shooting technique cum Runge-Kutta method to exploit this system of nonlinear ordinary differential equations with boundary value solver using the MATLAB program. Figure 2 depicts the flowchart of the numerical operation performed by the boundary value problem in MATLAB. Before writing code, it is necessary to make the following things.

$$f = f(1), f' = f(2), f'' = f(3), \theta = f(4), \theta' = f(5). \tag{16}$$

Using the assumptions (16) the following system of first order ordinary differential equations by using the equations (10-11) and the boundary conditions (12) are obtained.

$$f'(1) = f(2),$$

$$f'(2) = f(3),$$

$$f'(3) = \frac{1+Je}{\nu_{tf}/\nu_f}\left(-ff'' + \left(\frac{2m}{1+m}\right)(f')^2 - \left(\frac{2}{1+m}\right)Hae^{-\beta\eta}\right), \qquad (17)$$

$$f'(4) = f(5),$$

$$f'(5) = -\frac{\alpha_f\,\text{Pr}}{\alpha_{tf}(1+R)}\left(\left(\frac{2}{1+m}\right)\lambda\theta + f\theta'\right),$$

with the boundary conditions

$$fa(1) = \alpha_1\frac{1-m}{1+m},\ fa(2) = 1,\ fa(5) = -\left(\frac{2}{1+m}\right)^{1/2}\frac{k_f}{k_{tf}}Bi\left(1 - fa(4)\right),\ fb(2) = 0,\ fb(4) = 0. \qquad (18)$$

Run the above system and get the required results presented in graphical form after changing it to MATLAB code.
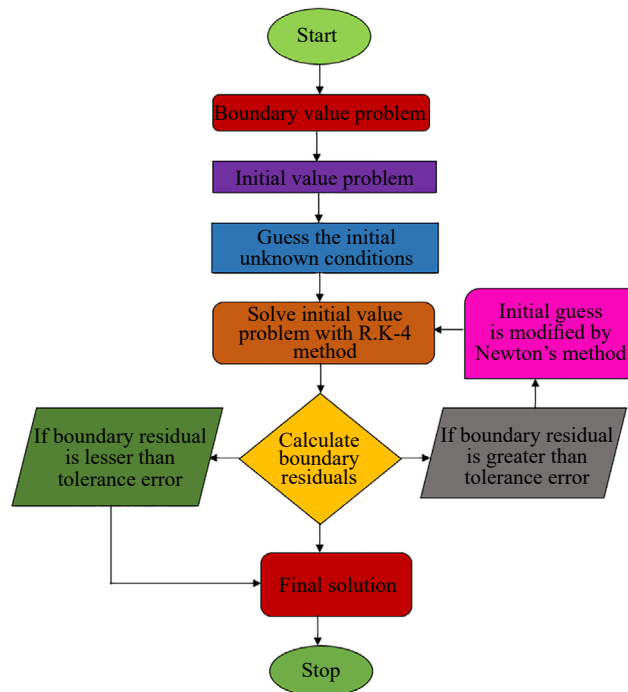
Figure 2. Flow chart of numerical procedure

4. Multiple linear regression for engineering quantities

Multiple linear regression is a statistical technique employed to examine the correlation between a minimum of two independent variables and a single dependent variable. The formula for multiple linear regression is expressed as follows:

$$y = c + c_1 x_1 + c_2 x_2 + c_3 x_3 + ... + c_n x_n. \tag{19}$$

Where 'x_i' independent variables, 'y' dependent variable, 'c' y-intercept, 'c_i' Regression coefficients of 'x_i' for i = 1, 2, 3, …, n. When determining the values of 'c_i' in the context of statistical analysis, if the p-value is found to be less than 0.05, it indicates that the relationship between y and x_i is considered statistically significant.

The present study employs the below models to investigate the correlation between the engineering parameters of interest, such as heat exchange rate, and the characteristics as

$$Cf_x = c + c_1 Je + c_2 m + c_3 Ha + c_4 \beta + c_5 \alpha_1. \tag{20}$$

$$Nu_x = d + d_1 Pr + d_2 m + d_3 Bi + d_4 \lambda + d_5 R. \tag{21}$$

The parameters which affect the momentum equation that are considered in skin friction, and which affect the temperature are considered in Nusselt number equation. From MATLAB, we have collected 9 sets of values for skin friction and Nusselt number to do regression analysis. Thus, we got the below outputs:

$$Cf_x = -0.6797 - 0.34499 Je - 1.0260 m + 4.0391 Ha - 1.41297 \beta - 0.0920 \alpha_1. \tag{22}$$

$$Nu_x = 2.3700 + 0.4022 Pr + 3.7748 m - 8.7162 Bi - 5.1613 \lambda - 0.8192 R. \tag{23}$$

5. Discussion on outcomes

Several control variables that surface in this investigation have been changed in this segment to examine their effects on the momentum and thermal profiles of the trihybrid nanofluid. Tables, graphs, and figures have all been used to display the outcomes. Fixing the relevant parameter values ($Pr = 6.2$, $Je = 4$, $\alpha_1 = 3.5$, $\beta = 0.6$, $Bi = 0.01$, $R = 3$, $m = 0.4$, $Ha = 0.8$, $\lambda = 0.5$) and using Tables 1 and 2 allows us to comprehend the problem's physics. Figure 3 and Figure 4 show the velocity profiles as an index of m for scenarios $\alpha_1 = 0$ and $\alpha_1 \neq 0$. The figures clearly show that when $\alpha_1 \neq 0$, the velocity is negatively impacted by elevation in m. The fluid's velocity increases as the elevation in m. This variation of the velocity profile is caused by fluid deformations when m increases the stretching speed of the Riga plate. The width of the velocity boundary layer increases as well. In this situation $\alpha_1 = 0$, there is a reverse trend in velocity. Figure 5 illustrates the effects of physical parameter Je, the proportion of relaxation to retardation time on velocity. As Je increases, the velocity of fluid decreases. Figure 6 shows that raising α_1 values decrease the width of the velocity boundary layer and the momentum profile. This is due to growing α_1 restricted stretching velocity, and the reason for maximum velocity near the plate may be physically read as an assist of the no-slip boundary specifications. Figure 7 shows that when β values rise, both the velocity profile and the corresponding boundary layer diminish. Figure 8 shows the impact of modified Hartmann number Ha seems to improve the profile of velocity. This profile may be caused by raising values of the modified Hartmann number, which strengthens the fluid-regulating external electric field. It can be seen in Figure 9, that the fluid's temperature profile rises noticeably for $\alpha_1 \neq 0$ when the velocity power index is less than or equal to 1. Physically, the varying thickness of the stretching sheet clarifies that the temperature magnitude is larger near the Riga plate for each increased value of the velocity power index.

In Figure 10 when $\alpha_1 = 0$, the distribution is inverted. The impact of Je on the temperature profile is seen in Figure 11. The temperature boundary layer spreads as Je rises. But for larger values of the wall thickness parameter, we obtain conflicting profiles shown in Figure 12. As we raise the wall thickness parameter, the temperature distribution decreases because less heat is transported from the plate to the fluid. As a result, with higher values of the wall thickness parameter, a decreasing temperature profile is shown. The existence of a robust magnetic field, characterized by a high Hartmann number, has the potential to decrease the heat transfer shown in Figure 13. This phenomenon arises from the damping influence exerted by the magnetic field on the motion of the liquid. Figure 14 illustrates the impact of R variability on the thermal profile. As R values increase, the temperature profile intensifies, with higher R values exerting a dominant influence on conduction. The system experiences a significant heat influx from radiation, leading to an

elevation in temperature. Because the Riga plate is convectively heated, the Biot number is critical in sculpting the temperature boundary layer. The heat exchange coefficient describes the convective heat exchange between the fluid and the wall. The heat exchange coefficient is heavily influenced by the thermal boundary conditions. As the Biot numerical values are increased, the heat transfer coefficient rises, resulting in greater thermal profiles shown in Figure 15. When expected, the thermal profiles in Figure 16 increase dramatically when the heat source parameter value increases. This is because greater values of the thermal source parameter raise the temperature of the fluid. In comparison to Newtonian and non-Newtonian fluids, (for $m = 0.4, 0.5, 0.6, 0.8, 1.0$ when $\alpha_1 \neq 0$) it is evident from Figure 17 and Figure 18 that the non-Newtonian fluid leads to drop in liquid velocity and rise in fluid temperature. This is because of the higher shear rate in the non-Newtonian fluid. Figure 19 and Figure 20 demonstrate the influence of escalating solid particle concentration on velocity and temperature components keeping the remaining parameters as constant. The velocity profile diminishes as the quantity of solid nanoparticles rises in the trihybrid nanofluid, a result attributed to increased collisions among the suspended nanoparticles. Conversely, temperature profiles exhibit improvement owing to the dissipation of energy in the form of heat by the nanoparticles. Furthermore, the appearance of chemical bonds among distinct nanoparticles suspended in the fluid contributes to an augmentation in heat exchange. Ultimately, this process leads to an enlargement of the thermal boundary layer thickness in the nanofluids.

Table 1. The thermophysical properties encompassing the base fluid and nanoparticles [31] used in this study

Physical parameters	H_2O	Al_2O_3	Cu	Ni
ρ (kg/m^3)	997.1	1,115	8,933	8,900
k (W/mK^3)	0.613	2,430	401	90.7
Cp (J/kgK)	4,179	0.253	385	444
μ (mPa/s)	0.891	-	-	-
Pr	6.2	-	-	-

Table 2. Equations of thermophysical properties of trihybrid nanofluid [31] used in this study

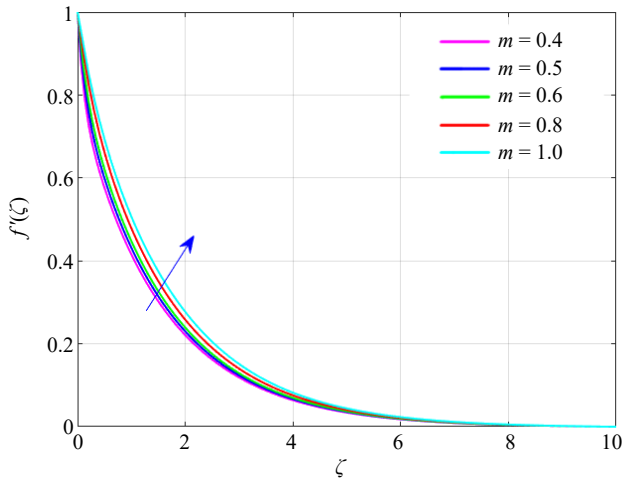| Properties	Trihybrid nanofluid
Dynamic Viscosity	$\mu_{tf} = \dfrac{\mu_f}{\left(1-\phi_1\right)^{2.5}\left(1-\phi_2\right)^{2.5}\left(1-\phi_3\right)^{2.5}}$
Density	$\rho_{tf} = \left(1-\phi_3\right)\{\left(1-\phi_2\right)[\rho_f\left(1-\phi_1\right)+\rho_1\phi_1]+\rho_2\phi_2\}+\rho_3\phi_3$
Heat capacity	$\left(\rho C_p\right)_{tf} = \left(1-\phi_3\right)\{\left(1-\phi_2\right)\left[\left(\rho C_p\right)_f\left(1-\phi_1\right)+\left(\rho C_p\right)_1\phi_1\right]+\left(\rho C_p\right)_2\phi_2\}+\left(\rho C_p\right)_3\phi_3$
Thermal conductivity	$K_{tf} = K_{hf}\left(\dfrac{K_3+2K_{hf}-2\phi_3\left(K_{hf}-K_3\right)}{K_3+2K_{hf}+\phi_3\left(K_{hf}-K_3\right)}\right)$ $K_{hf} = K_{nf}\left(\dfrac{K_2+2K_{nf}-2\phi_2\left(K_{nf}-K_2\right)}{K_2+2K_{nf}+\phi_2\left(K_{nf}-K_2\right)}\right)$ $K_{nf} = K_f\left(\dfrac{K_1+2K_f-2\phi_1\left(K_f-K_1\right)}{K_1+2K_f+\phi_1\left(K_f-K_1\right)}\right)$

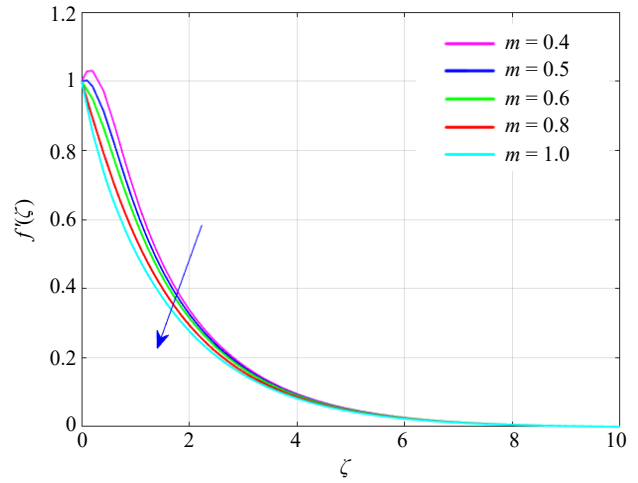**Figure 3.** Dominance of m on $f'(\zeta)$ when $\alpha_1 \neq 0$

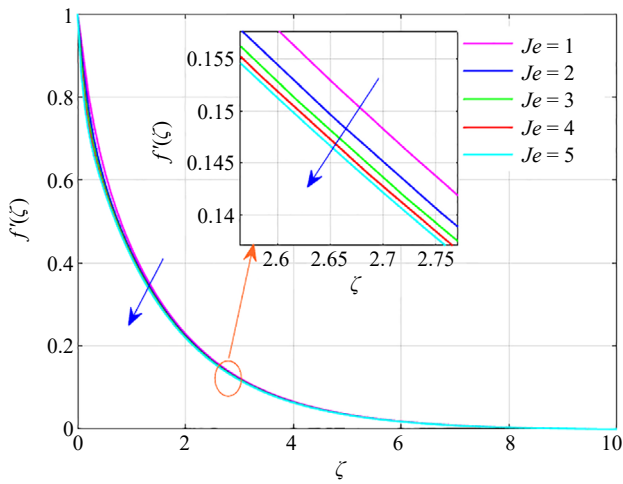**Figure 4.** Dominance of m on $f'(\zeta)$ when $\alpha_1 = 0$
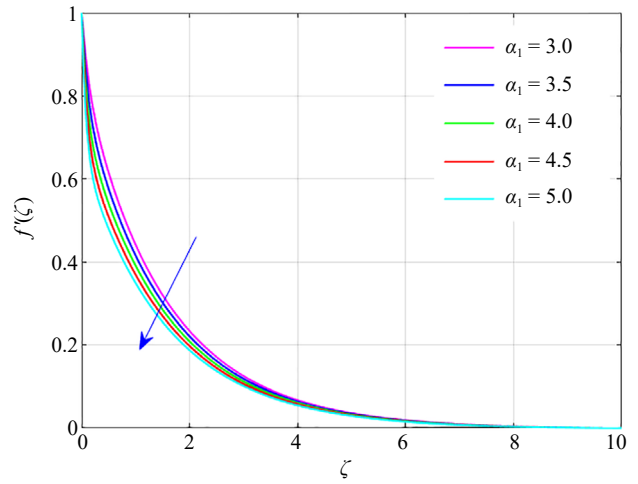

Figure 5. Dominance of Je on $f'(\zeta)$

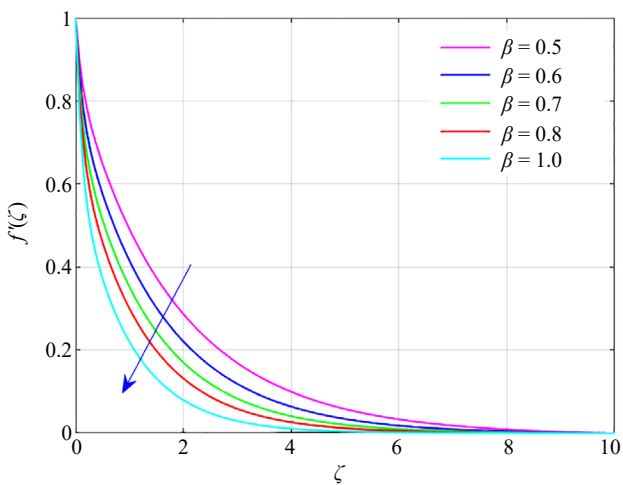**Figure 6.** Dominance of α_1 on $f'(\zeta)$

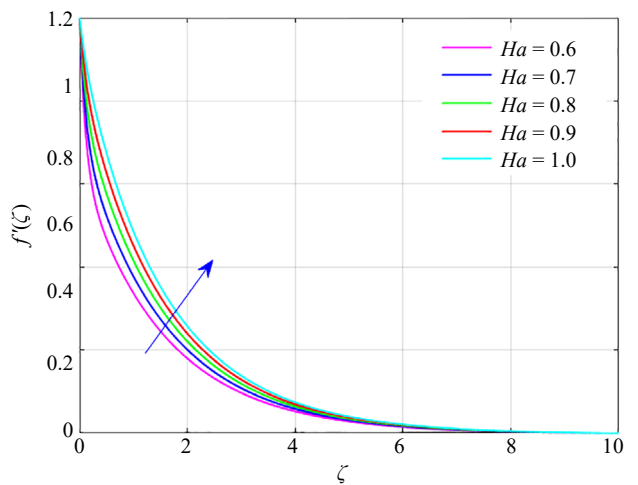**Figure 7.** Dominance of β on $f'(\zeta)$
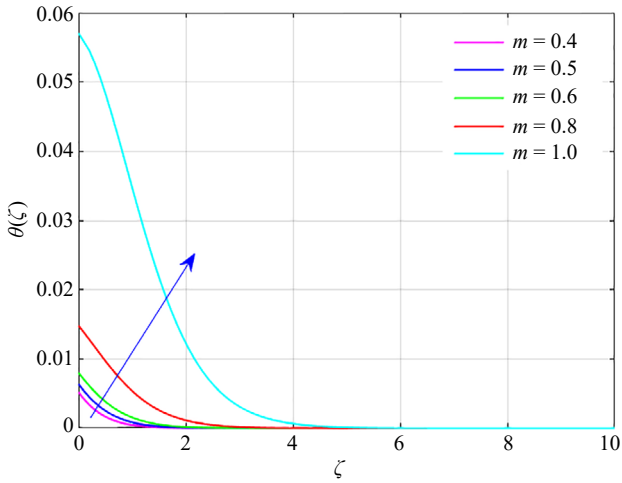

Figure 8. Dominance of Ha on $f'(\zeta)$

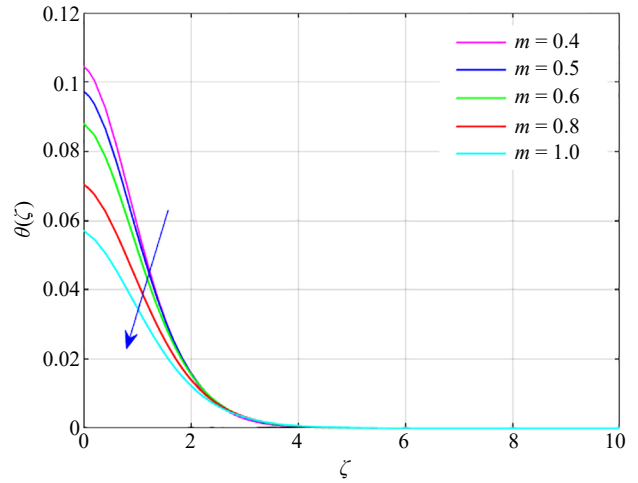**Figure 9.** Dominance of m on $\theta(\zeta)$ when $\alpha_1 \neq 0$

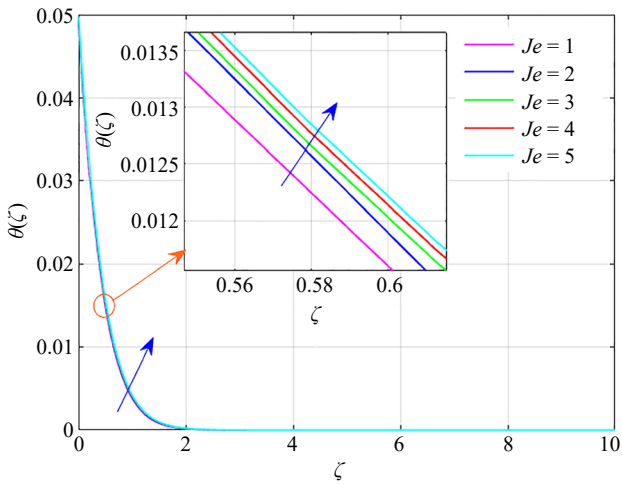**Figure 10.** Dominance of m on $\theta(\zeta)$ when $\alpha_1 = 0$
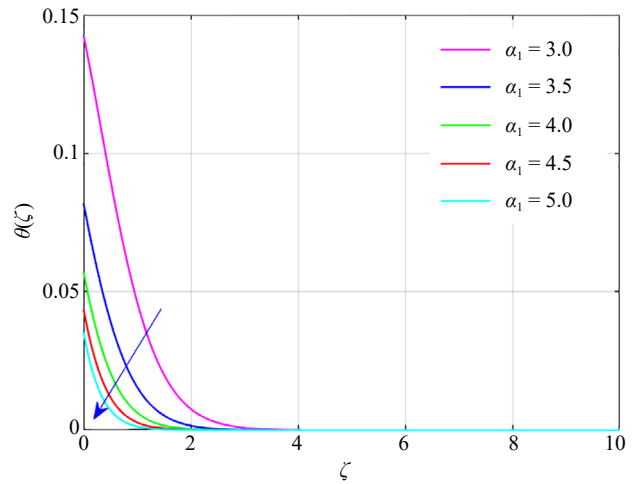

Figure 11. Dominance of Je on $\theta(\zeta)$

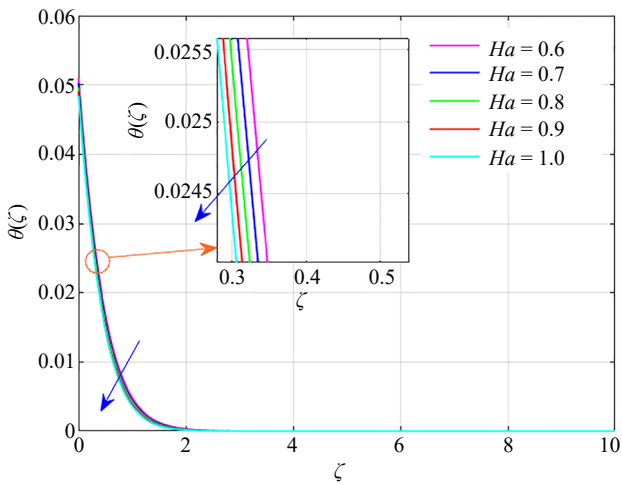**Figure 12.** Dominance of α_1 on $\theta(\zeta)$
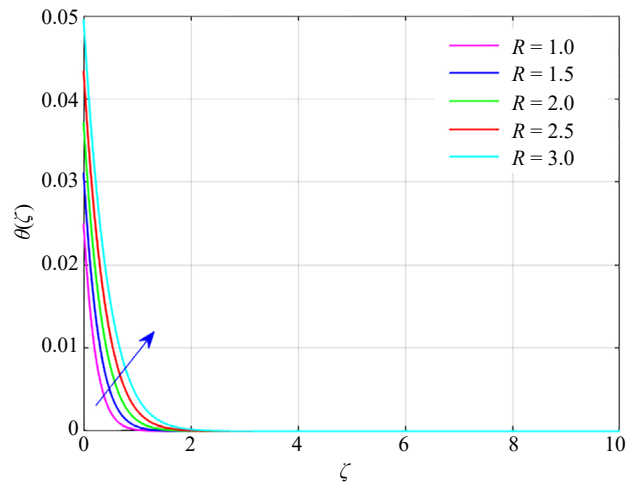

Figure 13. Dominance of Ha on $\theta(\zeta)$

Figure 14. Dominance of R on $\theta(\zeta)$
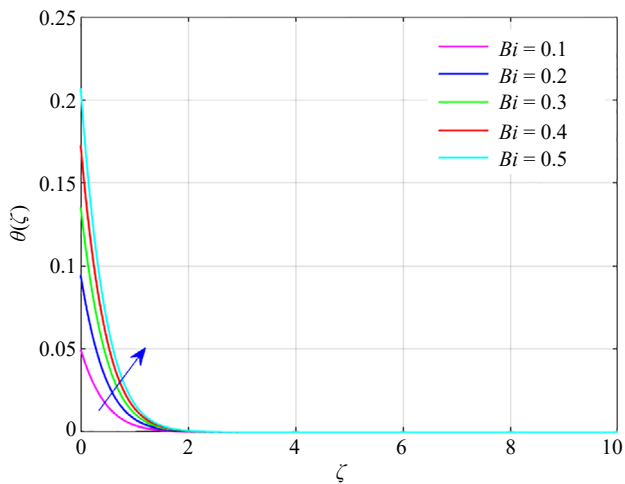
Figure 15. Dominance of Bi on $\theta(\zeta)$

Figure 16. Dominance of λ on $\theta(\zeta)$
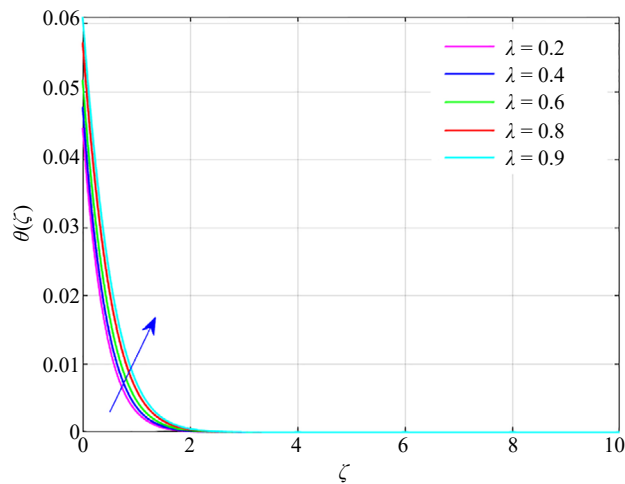
Solid: Non-Newtonian(Jeffery)
Dashed: Newtonian
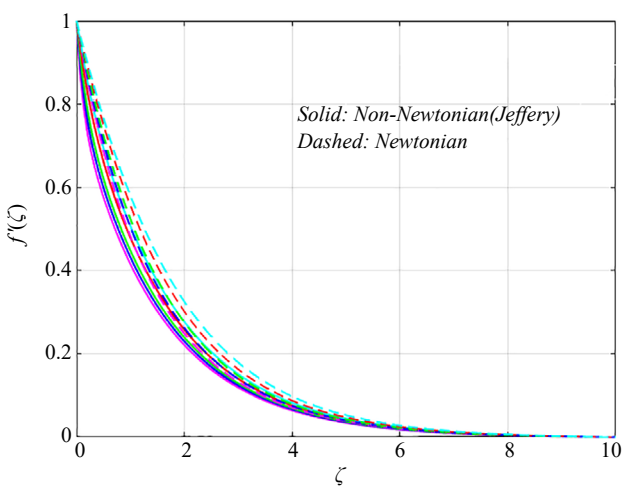
Figure 17. Comparison of $f'(\zeta)$

Solid: Non-Newtonian(Jeffery)
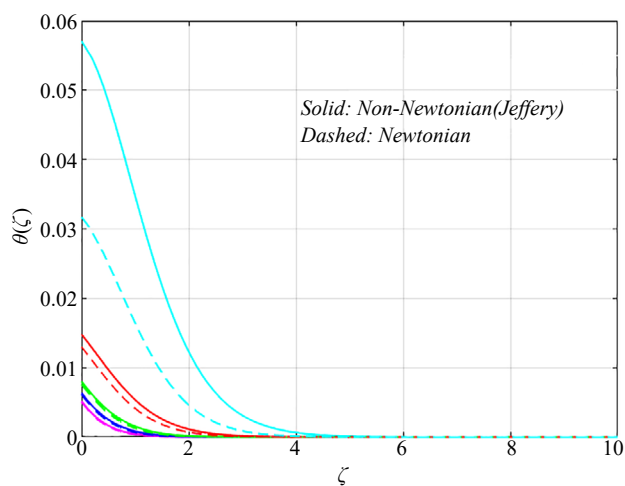*Dashed: Newtonian*

Figure 18. Comparison of $\theta(\zeta)$
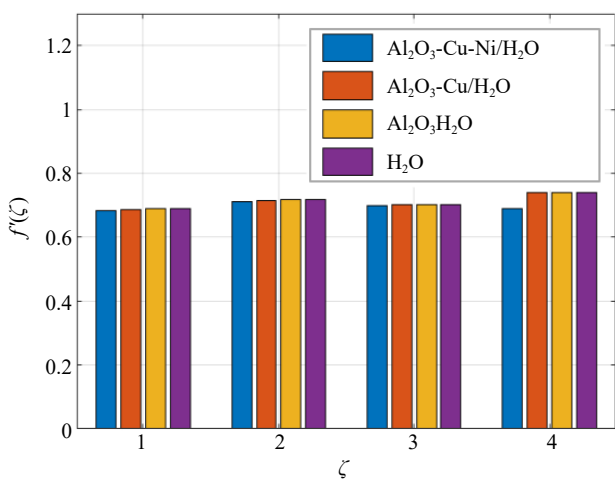

Figure 19. Comparison of $f'(\zeta)$
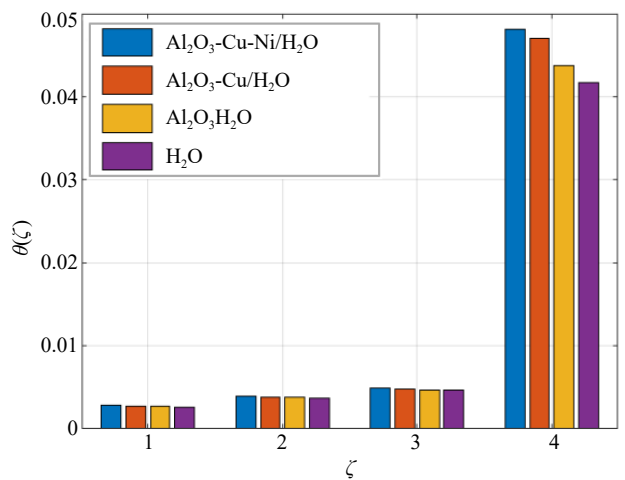

Figure 20. Comparison of $\theta(\zeta)$

<div align="center">**Table 3.** Regression analysis for skin friction</div>

Regression Statistics	
Multiple R	0.998242821
R Square	0.99648873
Adjusted R Square	0.990636614
Standard Error	0.016574011
Observations	9

<div align="center">**Table 4.** ANOVA for skin friction</div>

-	df	SS	MS	F	Significance F
Regression	5	0.233875	0.046775	170.2783606	0.000704209
Residual	3	0.000824	0.000275	-	-
Total	8	0.2347	-	-	-

<div align="center">**Table 5.** Coefficients of regression for skin friction</div>

-	Coefficients	Standard Error	t Stat	P-value	Lower 95%	Upper 95%
Intercept	-0.679676683	0.050974	-13.3338	0.00091176	-0.841898143	-0.51746
Je	-0.344989753	0.267189	-1.29118	0.287132434	-1.19530398	0.505324
m	-1.026000661	0.218346	-4.69897	0.018231656	-1.720874026	-0.33113
Ha	4.039095061	1.335597	3.024188	0.056570912	-0.211369481	8.28956
β	-1.412968438	0.471779	-2.99498	0.05790006	-2.914379036	0.088442
α_1	-0.091983129	0.143465	-0.64115	0.567041177	-0.548552536	0.364586

<div align="center">**Table 6.** Probability output for skin friction</div>

Percentile	Y
5.555555556	-0.75107
16.66666667	-0.543033
27.77777778	-0.423578
38.88888889	-0.363603
50	-0.336621
61.11111111	-0.275584
72.22222222	-0.256548
83.33333333	-0.241533
94.44444444	-0.23486

Table 7. Regression analysis for Nusselt number

Regression Statistics	
Multiple R	0.974242376
R Square	0.949148207
Adjusted R Square	0.864395219
Standard Error	0.044777088
Observations	9

Table 8. ANOVA for Nusselt number

-	df	SS	MS	F	Significance F
Regression	5	0.112269219	0.022454	11.198994	0.037169202
Residual	3	0.006014963	0.002005	-	-
Total	8	0.118284182	-	-	-

Table 9. Coefficients of regression for Nusselt number

-	Coefficients	Standard Error	t Stat	P-value	Lower 95%	Upper 95%
Intercept	2.370018339	2.308781626	1.026523	0.3801797	-4.97755522	9.717591895
Pr	0.402184753	0.245182614	1.640348	0.1994673	-0.37809575	1.182465259
m	3.774754861	7.711578872	0.489492	0.6580511	-20.7669308	28.31644055
Bi	-8.716242369	12.43098482	-0.70117	0.5336914	-48.2771841	30.84469933
λ	-5.161353263	2.615635627	-1.97327	0.1429909	-13.4854732	3.162766674
R	-0.819275048	0.966193495	-0.84794	0.4587642	-3.89413397	2.255583872

Table 10. Probability output for Nusselt number

Percentile	Y
5.555555556	0.03988
16.66666667	0.172129
27.77777778	0.255325
38.88888889	0.289464
50	0.291959
61.11111111	0.29908
72.22222222	0.384427
83.33333333	0.393601
94.44444444	0.435449

The probability plots of the friction factor and the Nusselt number are shown in Figures 21 and 22, respectively, presuming that the datasets that fall under investigation are normal distribution. It is possible to infer that the model appropriately represented the datasets fall under consideration for friction factor and Nusselt number based upon the adjusted-R^2 values displayed in Tables 3 and 7. Tables 4 and 8 show the regression model holds statistical significance due to P-values in the F-test that are below 0.05 for friction factor and the Nusselt number, respectively. Tables 5 and 9 present the regression coefficients for friction factor and Nusselt number, respectively. In friction factor, P-values (> 0.05) in the T-test indicate that the constants Je, m, Ha, β, and α_1 are statistically insignificant. In the Nusselt number, P-values (> 0.05) in the T-test indicate that the constants m, and Bi are statistically invalid, however, P-values (< 0.05) indicate that the parameters Pr, λ, and R are statistically valid. The probability output for friction factor and Nusselt number are shown in Tables 6 and 10.
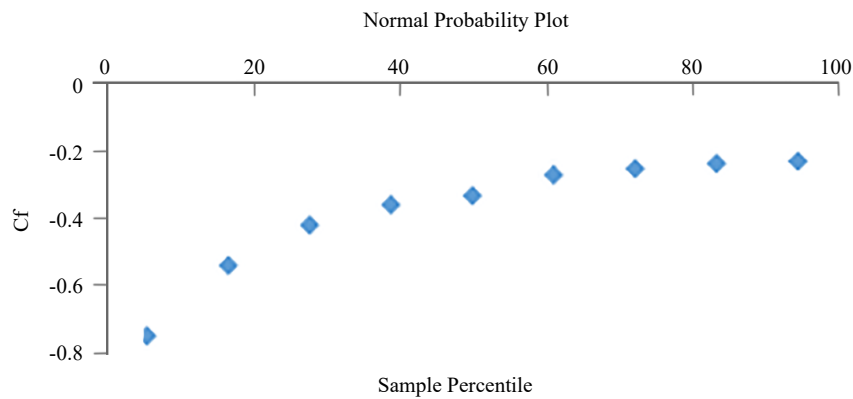

Figure 21. Probability plot for skin friction

Figure 22. Probability plot for Nusselt number
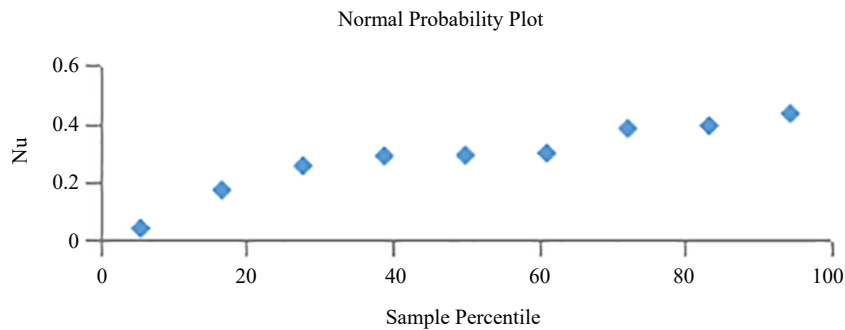
6. Validation

A comparison of our results with a previously published study by Thakur [31] was performed to validate the code and ensure the validity of the results. Table 11 shows several values of $-f''(0)$ for various values of m for $\alpha_1 = 0.25$ and $\alpha_1 = 0.5$ when $Pr = 6.2$ and that the current study's findings are quite similar to previously reported ones.

Table 11. A comparison for values of $-f''(0)$ for various values of m for $\alpha_1 = 0.25$ and $\alpha_1 = 0.5$ when $Pr = 6.2$

m	Thakur et al. [31]		Present study	
	$\alpha_1 = 0.25$	$\alpha_1 = 0.5$	$\alpha_1 = 0.25$	$\alpha_1 = 0.5$
10	1.1433	1.0603	1.14333	1.06034
9	1.1404	1.0589	1.14040	1.05893
7	1.1323	1.0551	1.13229	1.05506
5	1.1186	1.0486	1.11860	1.04862
3	1.0905	1.0359	1.09050	1.03588
1	1.0000	1.0000	1.00001	1.00001
0.5	0.9338	0.9799	0.93383	0.97995
0	0.7843	0.9576	0.78428	0.95764

7. Conclusions

This research introduces a computational mathematical model to analyze the flow of a (Al_2O_3-Cu-Ni/H_2O) trihybrid nanofluid, a variable-thickness Riga plate stretched and heated by convective heat with non-Newtonian fluid in the appearance of thermal radiation. The primary objective is to examine the influence of different physical parameters on the flow of this trihybrid nanofluid, particularly under conditions such as convectively heated Riga plate and non-flat plate geometry. The findings are depicted in graphs, tables, and results, demonstrating a compelling behavior of the trihybrid nanofluid under the specified circumstances. The present research indicates that the influences on trihybrid nanofluid are more pronounced compared to hybrid and nanofluids. Multiple linear regression has been employed in this study to analyze engineering parameters, encompassing factors such as heat exchange rate and friction factor. To assess the accuracy of the current findings, a validation process has been conducted, comparing the outcomes of the present study with those of previous investigations. In summary, the conclusions drawn from this study can be outlined as follows:

• The presence of radiation and uniform heat source improves the Nusselt number, physically this energy transfer improvement assists in higher solar collector efficacy; converts that energy to usable heat. System performance can be upgraded as this enhancement allows for lesser operating temperatures which interestingly reduces the energy loss in solar thermal systems.

• The Lorentz force provided parallel to the surface of the Riga plate, as well as the velocity power index (when $\alpha_1 \neq 0$), aid in the flow of the (Al_2O_3-Cu-Ni/H_2O) trihybrid nanofluid.

• As Je increases, the velocity of fluid falls due to the proportion of relaxation to retardation time on velocity.

• Fluid temperature rises with the rising values of radiation parameter.

• The temperature profile of the trihybrid nanofluid is more noticeable than the plots of hybrid nanofluid, nanofluid, and base fluid.

• Je, m, α_1, β have a negative influence on surface drag force whereas Ha had a positive influence.

• Pr, and m have a positive impact on the Nusselt number where as R, λ, and Bi had negative influences.

Authors contribution

Both the authors equally contributed to the formulation, solving the problem, analyzing the results, and framing the paper.

Data availability

The data that has been used is confidential.

Conflict of interest

The authors declare no competing financial interest.

References

[1] Hayat T, Fatima A, Muhammad K, Alsaedi A. Heat transfer and entropy analysis in squeezing flow of hybrid nanofluid (Au-CuO/NaAlg) with DF (Darcy-Forchheimer) and CC (Cattaneo-Christov) heat flux. *Materials Science and Engineering: B*. 2023; 288: 116150.

[2] Kumar MD, Raju CS, Alshehri M, Alkarni S, Shah NA, Ali MR, et al. Dual dynamical jumps on Lie group analysis of hydro-magnetic flow in a suspension of different shapes of water-based hybrid solid particles with Fourier flux. *Arabian Journal of Chemistry*. 2023; 16(8): 104889.

[3] Poornima T, Sreenivasulu P, Souayeh B. Mathematical study of heat transfer in a stagnation flow of a hybrid nanofluid over a stretching/shrinking cylinder. *Journal of Engineering Physics and Thermophysics*. 2022; 95(6): 1443-1454.

[4] Santhosh HB, Nagendramma V, Durgaprasad P, Mamatha SU, Raju CK, Raju KV. Dynamics of unsteady Carreau fluid in a suspension of dust and hybrid solid particles with non-Fourier and Fourier fluxes. *International Journal of Modern Physics B*. 2023; 37(29): 2350251.

[5] Rao AS, Sainath S, Rajendra P, Ramu G. Mathematical modelling of hydromagnetic casson non-Newtonian nanofluid convection slip flow from an isothermal sphere. *Nonlinear Engineering*. 2019; 8(1): 645-660.

[6] Rama Devi SV, Reddy MG. Analyzing the exponentially varying viscosity of micropolar carreau nanofluid flow with variable fluid properties in stretching porous sheet. *Journal of Nanofluids*. 2022; 11(5): 754-771.

[7] Khan MI, Shoaib M, Zubair G, Kumar RN, Prasanna kumara BC, Mousa AA, et al. Neural artificial networking for nonlinear Darcy-Forchheimer nanofluidic slip flow. *Applied Nanoscience*. 2023; 13(6): 3767-3786.

[8] Algehyne EA, Abdelmohsen SA, Gowda RP, Kumar RN, Abdelbacki AM, Gorji MR, et al. Mathematical modeling of magnetic dipole effect on convective heat transfer in Maxwell nanofluid flow: Single and multi-walled carbon nanotubes. *Waves in Random and Complex Media*. 2023; 33(2): 489-504.

[9] Mishra A, Kumar M. Influence of viscous dissipation and heat generation/absorption on Ag-water nanofluid flow over a Riga plate with suction. *International Journal of Fluid Mechanics Research*. 2019; 46(2): 113-125.

[10] Upreti H, Mishra SR, Pandey AK, Pattnaik PK. Thermodynamics analysis of Casson hybrid nanofluid flow over a porous Riga plate with slip effect. *International Journal for Multiscale Computational Engineering*. 2024; 22(5): 19-34.

[11] Upreti H, Pandey AK, Joshi N, Makinde OD. Thermodynamics and heat transfer analysis of magnetized Casson hybrid nanofluid flow via a Riga plate with thermal radiation. *Journal of Computational Biophysics and Chemistry*. 2023; 22(03): 321-334.

[12] Patil VS, Shamshuddin MD, Ramesh K, Rajput GR. Slipperation of thermal and flow speed impacts on natural convective two-phase nanofluid model across Riga surface: Computational scrutinization. *International Communications in Heat and Mass Transfer*. 2022; 135: 106135.

[13] Shamshuddin MD, Akkurt N, Saeed A, Kumam P. Radiation mechanism on dissipative ternary hybrid nanoliquid flow through rotating disk encountered by Hall currents: HAM solution. *Alexandria Engineering Journal*. 2023; 65: 543-559.

[14] Anwar MS. Numerical study of transport phenomena in a nanofluid using fractional relaxation times in Buongiorno model. *Physica Scripta*. 2020; 95(3): 035211.

[15] Hussain Z, Bashir Z, Anwar MS. Analysis of nanofluid flow subject to velocity slip and Joule heating over a nonlinear stretching Riga plate with varying thickness. *Waves in Random and Complex Media*. 2022; 1-7. Available from: https://doi.org/10.1080/17455030.2022.2124468.

[16] Revathi G, Sajja VS, Babu MJ, Srinivasa Babu KS, Suneel Kumar A, Raju CS, et al. Multiple linear regression analysis on the flow of ternary hybrid nanofluid by a quadratically radiated stretching surface with and second

order slip. *Waves in Random and Complex Media*. 2023; 1-8. Available from: https://doi.org/10.1080/17455030.2023.2181645.

[17] Zayan M, Rasheed AK, John A, Muniandi S, Faris A. Synthesis and characterization of novel ternary hybrid nanoparticles as thermal additives in H_2O. *Nanoscience*. 2021. Available from: https://doi.org/10.26434/chemrxiv.13710130.v1.

[18] Kumar V, Sahoo RR. Experimental and numerical study on cooling system waste heat recovery for engine air preheating by ternary hybrid nanofluid. *Journal of Enhanced Heat Transfer*. 2021; 28(4): 1-29.

[19] Algehyne EA, Arif M, Saeed A, Bilal M, Kumam P, Galal AM. Modified Buongiorno's model for the analysis of chemically reacting jet flow of ternary hybrid nanofluid under the influence of activation energy and bio-active mixers. *ZAMM-Journal of Applied Mathematics and Mechanics/Zeitschrift für Angewandte Mathematik und Mechanik*. 2023; 103(6): e202200498.

[20] Hayat T, Asad S, Mustafa M, Alsaedi A. MHD stagnation-point flow of Jeffrey fluid over a convectively heated stretching sheet. *Computers & Fluids*. 2015; 108: 179-185.

[21] Bilal S, Mamatha SU, Raju CS, Rao BM, Malik MY, Akgül A. Dynamics of chemically reactive Jeffery fluid embedded in permeable media along with influence of magnetic field on associated boundary layers under multiple slip conditions. *Results in Physics*. 2021; 28: 104558.

[22] Malleswari B, Pandikunta S, Bhaskar Reddy N. Electrical resistance heating distribution on three dimensional Jeffrey radiating nanofluid flow past stretching surface. *Journal of Computational & Applied Research in Mechanical Engineering (JCARME)*. 2022; 11(2): 339-349.

[23] Dharmaiah G, Mebarek-Oudina F, Kumar MS, Kala KC. Nuclear reactor application on Jeffrey fluid flow with Falkner-Skan factor, Brownian and thermophoresis, non-linear thermal radiation impacts past a wedge. *Journal of the Indian Chemical Society*. 2023; 100(2): 100907.

[24] Garg A, Sharma YD, Jain SK. Stability analysis of thermo-bioconvection flow of Jeffrey fluid containing gravitactic microorganism into an anisotropic porous medium. *Forces in Mechanics*. 2023; 10: 100152.

[25] Alnahdi AS, Gul T. Hybrid nanofluid flow over a slippery surface for thermal exploration. *Advances in Mechanical Engineering*. 2023; 15(8): 16878132231190060.

[26] Poornima T, Sreenivasulu P, Souayeh B. Thermal radiation influence on non-Newtonian nanofluid flow along a stretchable surface with Newton boundary condition. *International Journal of Ambient Energy*. 2023; 44(1): 2469-2479.

[27] Ramesh K, Rawal M, Patel A. Numerical simulation of radiative MHD Sutterby nanofluid flow through porous medium in the presence of hall currents and electroosmosis. *International Journal of Applied and Computational Mathematics*. 2021; 7: 1-2.

[28] Zhang R, Ahammad NA, Raju CS, Upadhya SM, Shah NA, Yook SJ. Quadratic and linear radiation impact on 3D convective hybrid nanofluid flow in a suspension of different temperature of waters: Transpiration and fourier fluxes. *International Communications in Heat and Mass Transfer*. 2022; 138: 106418.

[29] Bhargavi N, Poornima T, Souayeh B. Magnetohydrodynamic conjugate heat transfer analysis on a viscous fluid past a vertical permeable plate. *International Journal of Modern Physics B*. 2023; 2450211. Available from: https://doi.org/10.1142/S0217979224502114.

[30] Hussain Z, Al-Khaled K, Ashrif U, Abbasi A, Khan SU, Farooq W, et al. A mathematical model for radiative peristaltic flow of Jeffrey fluid in curved channel with Joule heating and different walls: Shooting technique analysis. *Ain Shams Engineering Journal*. 2022; 13(5): 101685.

[31] Thakur A, Sood S. Trihybrid nanofluid flow towards convectively heated stretching riga plate with variable thickness. *Journal of Nanofluids*. 2023; 12(4): 1129-1140.